PAPER • OPEN ACCESS

A quantitative study of the dynamic response of compliant microfluidic chips in a microfluidics context

View the article online for updates and enhancements.

A quantitative study of the dynamic response of compliant microfluidic chips in a microfluidics context

Marie Hébert, **Jan Huissoon** and **Carolyn L Ren**[*]

Mechanical and Mechatroncis Engineering, University of Waterloo, 200, University Avenue West, Waterloo, Ontario, Canada

E-mail: c3ren@uwaterloo.ca

Abstract

Polydimethylsiloxane (PDMS) is a widely used material for microfluidic devices due to its low cost, superior optical properties and fast iterative design process. Its softness however creates challenges for the device design and operation because part of the applied pressures contributes to deform chips instead of controlling the flow. The resulting dynamic behaviour is often ignored in passive microfluidic that focuses on the static behaviour of the chip, however, can cause low accuracy to active microfluidic that actuates flow frequently. Therefore, understanding the dynamic behaviour of microfluidic devices due to material compliance is of fundamental and practical importance. In this study, the microfluidic chip compliance is carefully considered by separating it from the sample tubing compliance. The capacitance is retrieved by assuming a symmetric RC circuit based on the experimentally determined time constant and chip resistance. The experimental capacitance is compared to a theoretical formula for chip designs with different height-to-width ratios and height-to-length ratios and for various fluids. The accuracy is within one order of magnitude that is much closer than previous approximations.

Supplementary material for this article is available online

(Some figures may appear in colour only in the online journal)

1. Introduction

1.1. Microfluidic context

Precise control of fluid flow at the micrometer scale is critical to the design and operation of microfluidic devices, which offer shorter reaction time and lower reagent consumption as compared to their traditional counterparts. These advantages are leveraged in numerous applications ranging across numerous fields such as biomedical assays (Fu *et al* 2015, Shembekar *et al* 2016, Kim *et al* 2021, Liu *et al* 2021), water quality (Lefevre *et al* 2012, Patinglag *et al* 2019, Waghwani *et al* 2020), drug screening (Courtney *et al* 2016), materials (Luo *et al* 2019), and many more.

The applications use a variety of microfluidic platforms. The capabilities of both passive and active platforms have been demonstrated in application-based studies. However, the independent use by end-users is still limited. This is attributed to the knowledge barrier faced by users in addition to the robustness of the microfluidic platforms that should be improved. The barrier becomes more difficult to overcome when working

---

[*] Author to whom any correspondence should be addressed.

with droplet microfluidics because of its complex two-phase flow nature and high speed of droplet generation and manipulations that leaves almost no room for design and operation errors.

Active platforms are envisioned to palliate the robustness issues of certain microfluidic platform (Zhang *et al* 2021, Hebert *et al* 2022) because they normally work with simple geometries, which largely reduces the risks of fabrication defects and the need to balance flow resistance of a complex channel network involving droplets. Moreover, the active components handle microfluidic-related knowledge. As a result, the end-users are expected to more easily adopt microfluidic platforms to leverage their advantages without the need of extensive microfluidics knowledge such as precise balance of flow resistance of a channel network. Among the various active microfluidic platforms, the one presented by Wong and Ren (2016) offers unique advantages because it enables active control of individual droplets without the need to incorporate external forces. This method relies on the visual feedback of droplet position to actuate the pressure source for flow control and thus achieving droplet manipulations using a few T-junctions.

1.2. Motivation

Although this active control platform is promising, the accuracy of its controller needs to be largely improved. The controller calculates the required pressures for manipulating droplets based on the fluids theories and the visual feedback of the current droplet position (Wong and Ren 2016). In the controller, the dynamics of the microfluidic chip due to material compliance is not accounted for, which is not completely valid for microfluidic chips made of soft polydimethylsiloxane (PDMS), a widely used chip material for microfluidic applications. For example, part of the applied pressure is used to deform the chip instead of controlling the flow. As a result, the calculated pressures are further away from the needed pressures for achieving certain droplet manipulations. Therefore, a better understanding of the dynamics of the microfluidic chip contributed by material compliance is envisioned to provide better accuracy. Moreover, better understanding the dynamics of the microfluidic chip can provide insights for chip design.

1.3. Literature overview

The dynamic behaviour of the microfluidic chip is seldom studied in the literature. The passive systems that operate at steady state disregard transient behaviours. These transient behaviours inform the dynamic response of the microfluidic chip system. For active control, the actuation is periodically adjusted; small scale dynamics matters. The relative softness of PDMS-based chips is well known in the field. In addition to change in dimensions due to swelling, the walls of the channel deform under pressure. A study particularly looked at the additional flow rate resulting from the top wall deformation (Christov *et al* 2018). However, the derivation is restricted to 'shallow' microfluidic channels that have a much larger width than height. Furthermore, the comparison with experimental

data is for an upper wall thickness of 0.2 mm. Nevertheless, the demonstration of the importance of channel deformation for static flow further motivates the investigation of its dynamic effects.

The model-based controller in the work by Wong and Ren (2016) relied on a formulation of the capacitance as per equation (1) that proved sufficient for stable operation. However, the formula is not experimentally verified specifically for the capacitance.

$$C = \left(\frac{A}{\kappa} + \frac{l}{\beta}\right) A \qquad (1)$$

where A is the cross sectional area (m²), $\kappa(A_{\text{substrate}}, E, l) = A_{\text{substrate}} E / l$ is the substrate stiffness (Pa · m), $A_{\text{substrate}}$ is the substrate area (m²), E is the elastic modulus of the substrate material (Pa), l is the channel length (m), and β is the adiabatic bulk modulus (Pa). Note that the channel cross-section area (A) is multiplied to the original formula to align with the other references that consider the flow rate rather than the velocity.

Under the assumption of small deformations, the microchannel of rectangular cross-section is approximated as per equation (2) (Cartas Ayala 2013). Although the equations are presented within the context of a manometer design, they are deemed pertinent. This equation is indirectly verified through hydrodynamic resistance experiments. Nevertheless, the context of the active droplet control platform motivates a deeper and more thorough consideration of the rectangular channel capacitance.

$$C = \frac{\alpha^* \, w \, h \, l (1 + \nu)}{E} \qquad (2)$$

where C is the rectangular channel capacitance (m³ Pa⁻¹), α^* is a scaling factor depending on the width-to-height ratio with maximum value of 1 ( ), w is the channel width (m), h is the channel height (m), l is the channel length (m), ν is the Poisson's ratio of the material [ ], and E is the elastic modulus of the material (Pa).

2. Methodology

The experiments collect the applied pressure and resulting flow rate at a 1 kHz sampling rate. The objective is to determine the dynamics between the pressure and flow rate using a first-order transfer function fit in *Matlab*.

2.1. Microfluidic chip fabrication

The micro-fabrication process follows a standard procedure that is detailed in the literature (Qin *et al* 2010). The soft lithography procedure requires a master. The fabrication involves the two-step spin coating of SU-8 2005 and SU-8 2025 on a silicon wafer.

The PDMS chip is moulded using the master. Although hydrophobic surface properties are not required because the tests are single-phase, a similar process is followed to ensure similar mechanical properties (Johnston *et al* 2014,
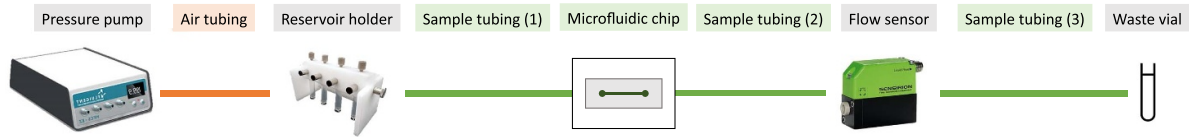
Figure 1. Experimental setup schematic for data collection with the microfluidic chip before the flow sensor.

Wang *et al* 2014). The mould is cured at 95 °C for 1 h before bonding to a PDMS-coated glass slide using oxygen plasma. Then, the chip is baked at 170 °C for at least 24 h.

The mechanical properties of the PDMS chip are maintained constant throughout the experiments. Consequently, the weight ratio of the pre-polymer and cross-linker is maintained at 10–1. More specifically, the 95% confidence interval of the weight ratio is (9.95, 10.00).

2.2. The impact of the flow sensor and sample tubing dynamics

The dynamics of the flow sensor and the sample tubing are experimentally defined to isolate the dynamics of the microfluidic chip. The details are provided in supplementary information S1.

In summary, a pressure sensor (*TE Connectivity U536D-H00015-001BG*) and a flow rate sensor (*Sensirion SLI-430*) are used. Both system outputs are measured at a sampling rate of 1 kHz. The flow rate sensor is calibrated for each of the fluids considered (water, silicone oil 5 cst, 20 cst and 50 cst).

The dynamics associated with the sample tubing is independently assessed. No microfluidic chip is present in the system for this series of experiments. Different tubing variables are considered: the tubing length and inner diameter. The time constant is experimentally determined for all fluids. The selected tubing has a inner diameter of 0.020" and a length of 0.769 m. The time constant is only significant for silicone oil 20 cst and 50 cst.

2.3. Inlet design

The tubing is connected through a press fit for the 1/16" outer diameter to the PDMS chip. The inlet then transitions to the micro-channel. The contribution of the inlet to the time constant is not separately considered. However, microfluidic chips require the inlet to easily connect the sample tubing. Therefore, the time constant with the inlet is considered representative of the usual microfluidic chip use.

The time constant associated with the inlet is the product of the resistance and the capacitance. However, the much wider inlet comparatively reduces the contribution to insignificant levels through a small resistance. Nevertheless, the area is expected to be between 10% and 500% of the channel area depending on the dimensions. The area of the inlet is about $5 \times 10^6\,\mu m^2$. For the smallest channel and the worse case, the width is 100 μm and the length is 10 mm for a total area of $1 \times 10^6\,\mu m^2$.

2.4. Experimental setup for data collection

The setup to collect data with the microfluidic chip is similar to the one shown in figure S1.2 in the supplementary material. The microfluidic chip can be located either before or after the flow sensor. If the chip is located after the flow sensor, the shape of the response will have one zero and one pole. Oppositely, when the chip is located before the flow sensor, the response will correspond to the typical first-order system response with no zeros and one pole. For simplicity, the latter setup is selected and is illustrated in figure 1.

The time constant is identified from the experimental data. However, the capacitance of the microfluidic chip is of interest. In order to relate the time constant to the capacitance, the resistance is required. The resistance of the chip itself is isolated from the total system resistance by considering the resistance of the system without the chip. A #10–32 union replaces the chip as per figure 1 to link sample tubing 1 and 2. The base resistance of the system is determined from an applied constant pressure and resulting flow rate as per equation (3) (Bruus 2008).

$$\Delta P = R \cdot Q \qquad (3)$$

where ΔP is the pressure different (Pa), R is the resistance (Pa· s · m^{-3}), and Q is the flow rate (m^3 s^{-1}).

The microfluidic chip is primed with a constant pressure of at least 250 mbar for 10 min before data collection. This allows the PDMS to swell and ensures the dimension are consistent for the duration of the data collection. After the priming phase, a constant pressure of 200 mbar is applied to record the flow rate. The base resistance of the system–including the sample tubing and flow sensor–is deducted from the overall system resistance to isolate the microfluidic chip resistance. The resistance is later used to get the chip capacitance from the time constant.

A series of 8 increasing and decreasing step functions from 0 to 200 mbar is then applied. The input pressure and output flow rate are recorded with a 1 ms time resolution. Consequently, the smallest time constant that the system can confidently identify is 10 ms. The series of steps is applied to multiple chip designs with repetitions with two different chips on two different days. The time constant is expected to vary based on three main factors: fluid viscosity, height-to-width ratio, and height-to-length ratios. Equation (4) combines the resistance (Bruus 2008) for a rectangular cross-section with the capacitance (Cartas Ayala 2013) of equation (2).

$$\tau = \left(\frac{12\,\mu l}{wh^3\left(1 - \frac{h}{w}\right)} \right) \cdot \left(\frac{\alpha^*\,w\,h\,l(1+\nu)}{E} \right). \qquad (4)$$

Table 1. Length-to-height ratios with corresponding dimensions.

Length-to-height ratio (l/h)	Length (l) (mm)	Height (h) (μm)
200	10	50
300	15	50
600	30	50
1500	45[a]	30
2500	75[a]	30
3000	90[a]	30

[a] Includes one curvature on the standard 1" X 3" glass slide.

Table 2. Specification of the length-to-height ratio considered for each fluid. (The X indicates the selected combination of fluid and length-to-height ratio. The — indicates the combination is not included in the paper).

	Length-to-height ratio					
Fluid	200	300	600	1500	2500	3000
Silicone oil 50 cst	X	X	X	—	—	—
Silicone oil 20 cst	X	X	X	—	—	—
Silicone oil 5 cst	X	X	X	—	—	—
Water	—	—	—	X	X	X

Simplifying equation (4), rearranging, and assuming that α^* is only a function of the height-to-width ratio $\left(\alpha^* = \alpha^*\left(\frac{h}{w}\right)\right)$ yields the following relationship for the time constant. The different parts of the equation are labelled according to the factor determining its value.

$$\tau = 12 \cdot \underbrace{\left(\frac{1+\nu}{E}\right)}_{\text{material}} \cdot \underbrace{(\mu)}_{\text{fluid}} \cdot \underbrace{\left(\frac{l}{h}\right)^2}_{\text{length}} \cdot \underbrace{\left(\frac{\alpha^*}{1 - 0.63\,\frac{h}{w}}\right)}_{\text{width}}. \quad (5)$$

For this experimental study, only the fluid, length-to-height ratio and height-to-width ratio are investigated. Four different fluids are considered: water, and silicone oil 5 cst, 20 cst and 50 cst. Water and silicone oil are typical dispersed and continuous phases used in microfluidic. Moreover, silicone oil is available with a range of viscosity. The height-to-length ratio ranges from 200 to 3000. The total channel length is restricted by the footprint available on a typical 1" X 3" glass slide. Moreover, typical channel heights of 30 μm and 50 μm are used. Table 1 specifies the height and length combinations for the six different length-to-height ratios. Furthermore, the height-to-width ratio is varied for each of the length-to-height ratio: $\frac{1}{10}$, $\frac{1}{6}$, $\frac{1}{4}$, and $\frac{1}{2}$.

Only certain fluids are tested with each length-to-height ratio. The expected time constant informs whether the information is useful. For example, for smaller length-to-height ratios, the time constant is expected to decrease. Thus, for water, the higher length-to-height ratios are selected. Table 2 summarizes which length-to-height ratios are considered for each fluid. Larger length-to-height ratios for silicone oil results in a flow rate too small to measure with the flow sensor. Smaller length-to-height ratios for water saturates the flow sensor at its maximum flow.

2.5. Assumptions for the time constant

The time constant resulting from this methodology is attributed to the compliance of the microfluidic chip. Other factors are disregarded and are compensated for as follows.

The input pressure is measured directly at the reservoir holder. Nonetheless, a small pressure offset from the hydrostatic pressure of the fluid in the vial occurs. However, the maximum height variation is 30 mm which corresponds approximately to 3 mbar. Consequently, this is neglected and lumped with the other system uncertainties.

The time constant associated with the sample tubing was investigated. Hence, the time constant can be compensated for to isolate the contribution from the microfluidic chip itself. Figure S1.3(d) in the supplementary material shows that for a viscosity smaller than 5 cst—thus for water and silicone oil 5 cst—the time constant is negligible compared to the system minimal time constant identifiable of 10 ms. For silicone oil 20 cst and 50 cst, the time constant is accurately identified for increasing and decreasing steps.

As for the other dynamics associated with the microfluidic chip itself, there is inductance and compliance from fluid compressibility. For inductance, the small characteristic length of the micro-channel unsurprisingly means negligible inertial effects. Furthermore, a quick calculation with the worst-case scenario under study confirms the relatively small scale of the associated time constant. Thus, inductance is not considered.

$$\tau_{LR} = \frac{L}{R} = \frac{\rho l}{wh} \cdot \frac{wh^3(1 - 0.63\,\frac{h}{w})}{12\,\mu l} = \frac{h^2(1 - 0.63\,\frac{h}{w})}{12\,\eta} \quad (6)$$

$$\tau_{LR} < \frac{(50 \times 10^{-6})^2(1 - 0.63 \cdot 0.1)}{12 \cdot 1 \times 10^{-6}} < 0.2\,\text{ms}. \quad (7)$$

As for the compliance contributed by the fluid compressibility comparatively to the material deformation, the adiabatic bulk modulus of the fluids (β) and elastic modulus of PDMS (E) are compared. The order of magnitude of GPa is considered for the adiabatic modulus and a typical value of 2 MPa is used for the PDMS elastic modulus. Thus, the contribution from the fluid compressibility is only about 0.2% of the material deformation. Consequently, the compressibility is neglected, and only the material deformation is considered.

2.6. Data processing

The data is processed first by converting the recorded values to pascals (Pa) and meters cubed per second (m³ s⁻¹) for the pressure sensor and flow sensor respectively. The series of eight increasing and decreasing steps is then separated into smaller subsets of input and output data. The output flow rate is offset using the average of the first 1000 data points. Thus, the change in flow rate is considered for the first-order model fit.

Then, the *Matlab* function `tfest` is used to fit a transfer function with no zeros and one pole. The time constant (τ) is obtained from the denominator coefficients. When using silicone oil 20 cst or 50 cst, the time constant of the tubing must be compensated for using the data from figure S1.3(d) in the

supplementary material. The time constant of the chip is identified through a lookup table built using a combined system with the time constant of the tubing and an arbitrary time constant covering the desired range. Then, a first-order system is fit to the combined first-order systems. Based on that identified first-order system time constant and the tubing time constant, the time constant of the chip is retrieved.

The time constant of the chip (τ_{chip}) considers both its resistance (R_{chip}) and its capacitance (C_{chip}). The resistance is previously determined using constant pressure-driven flow. Thus, the capacitance is calculated from the resistance and the time constant as per equation (8). A symmetric circuit analogy with half of the resistance distributed on either side of the capacitance is used. This is privileged over the simpler RC circuit for the symmetry of the response that corresponds better to the physical system.

$$C_{chip} = 4 \, \frac{\tau_{chip}}{R_{chip}}. \tag{8}$$

3. Results and discussion

The calculation of the capacitance compensates for the variations in resistance from the nominal values. The time constant plots are omitted. Two first-order fit data sets are shown in figure 2. This case is for a smaller flow rate that exhibits a smaller signal-to-noise ratio. However, the first-order function averages the noise and nevertheless provides an acceptable fit.

As expected, the capacitance decreases with an increasing height-to-width ratio; in other words, the more square cross-section has a lesser capacitance than an elongated cross-section. The relationship is more or less inversely proportional ($C \propto \frac{1}{h/w}$). The mean capacitance for the various height-to-width ratios, length-to-height ratio, and fluid used are regrouped in figure 3. Each data point is an average of at least 60 increasing step and 60 decreasing step capacitance. Moreover, the two series for the same nominal length-to-height ratio are from two different chips on two different days. Error bars are omitted due to the relatively large discrepancy between the increasing and decreasing step capacitance.

3.1. Comparison with previous models

The capacitance of the microfluidic channel considered by previous work is given by equation (1). However, the experimental data significantly disagrees with the previous equation. The difference is five orders of magnitude ($O(10^{-20})$ vs. $O(10^{-15})$).

Consequently, an another form for the capacitance equation is considered (equation (2)). The fitting parameter (ϕ) allows for the adjustment of the capacitance based on the geometry. Without the fitting parameter, the discrepancy between the experimental values and the capacitance using equation (2) is one order of magnitude ($O(10^{-16})$ vs. $O(10^{-15})$). Although the prediction value is in closer agreement with the experiment value, the fitting parameter enables a more accurate prediction.
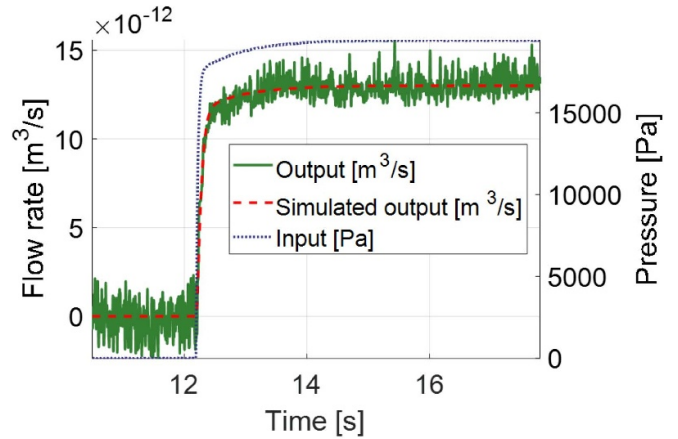
(a) Increasing step.
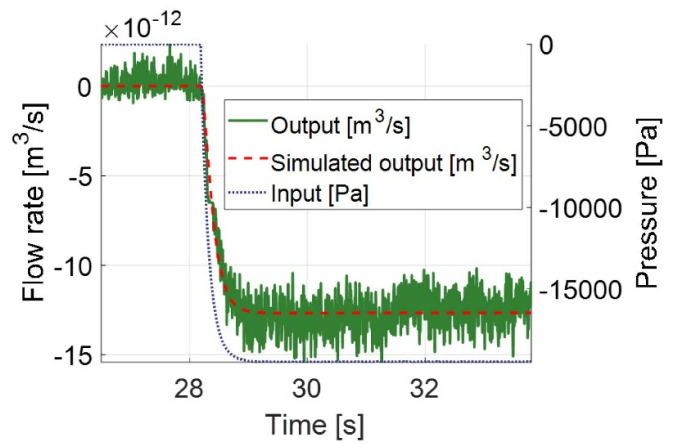
(b) Decreasing step.

Figure 2. First-order fit of the flow rate based on the measured pressure.

3.2. Fitting parameter (ϕ)

The fitting parameter (ϕ) compensates for the assumptions and simplifications leading to the discrepancy between the predicted and experimental values. Its value is calculated by dividing the experimental capacitance by all other terms from equation (2).

$$\phi = C_{exp} \cdot \frac{E}{w \, h \, l(1 + \nu)}. \tag{9}$$

The material properties from the PDMS ratio and the chip thickness are maintained constant for all experiments. Consequently, the fitting parameter should only depend on geometric variables. However, other uncertainties increase the spread of the data. The inlet hole location varies as it is manually located and punched before bonding the chip. PDMS debris are present in various quantity and behaves differently from chip to chip; the debris are unavoidable as they arise from the insertion of the tubing in the inlet. Certain chip lengths (for length-to-height ratios of 1500, 2500, and 3000) needed to include a curve to accommodate the full channel length within the glass slide dimensions (1"X3"). Finally, the viscosity is
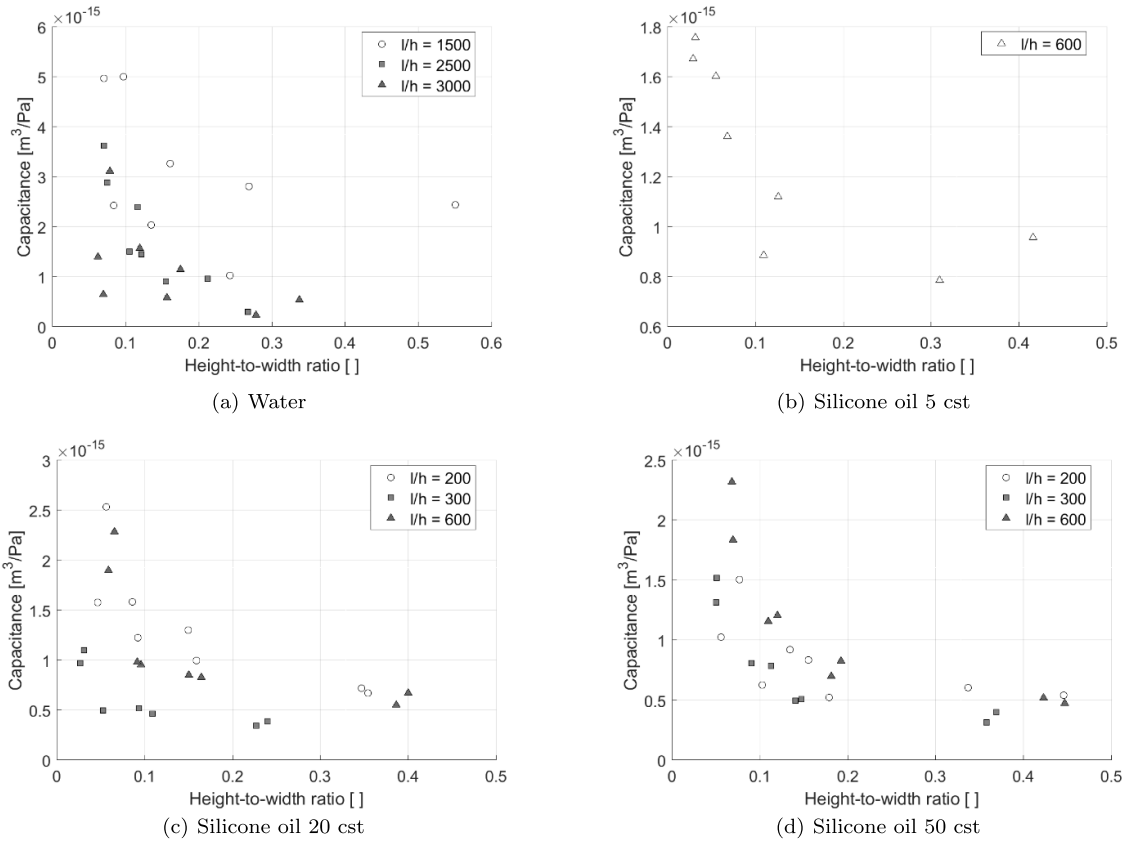
Figure 3. Capacitance results for the different fluids (water, and silicone oil 5 cst, 20 cst, and 50 cst) according to the height-to-width ratio.

varied to cover more conditions. However, the resistance compensation effectively negates any influence from the viscosity. Consequently, the only difference should be from geometry (height, width, and length). The correlation between alpha and the normalized width is weaker than for ϕ and the normalized length. The fitting parameter (ϕ), and thus, the capacitance, increases with an increasing height-to-length ratio. Longer channel lengths mean smaller flow rates and smaller additional flow from the deformation. Thus, the volume per pressure unit is also reduced, and hence, the capacitance is smaller.

When considering the capacitance trend per chip and per fluid (see figure 3), the relationship between the capacitance and the height-to-width ratio is clear. For an increased height-to-width ratio (or an increased 'squareness'), the capacitance decreases. However, the agglomeration of all results into the fitting parameter plot as a function of the height-to-width ratio (figure 4(a)) does not exhibit any clear trend. Oppositely, the relationship between the fitting parameter and the height-to-length ratio (figure 4(b)) demonstrates an approximately linear trend. Thus, the fitting parameter (ϕ) depends more strongly on the height-to-length ratio than on the height-to-width ratio.

The static deformation of the channel with the corresponding additional flow rate is dependent on the flow rate (and thus, indirectly, to the length) (Christov *et al* 2018). The additional flow rate from the deformation depends on the second term in the bracket. A large aspect ratio (i.e. wide channel) is assumed. The details of the derivation and assumptions are in the paper.

$$q \approx \frac{h_0^3}{12}\frac{w\Delta p}{\mu l}\left(1+\frac{3}{160}(w/t)^3(w/h_0)(\Delta p/E)\right) \quad (10)$$

where h_0 is the initial channel height (m), w is the channel width (m), Δp is the pressure difference across the channel (Pa), μ is the dynamic viscosity (Pa · s), l is the channel length (m), t is the top channel wall thickness (m), and E is the substrate elastic modulus (Pa).

Another study that is in contrast more experiment-based arrives to a similar conclusion (Gervais *et al* 2006). The additional flow rate depends on the initial channel height (h_0) and channel width (W), but not directly on the channel length. However, the dependence on the flow rate dictates a relationship to the channel length.

$$\frac{\Delta Q}{Q} = \frac{Q_{\text{deform}} - Q_{\text{rigid}}}{Q_{\text{rigid}}} \sim \frac{3}{2}\frac{\alpha}{E h_0}\frac{\Delta p W}{E h_0}, \quad (11)$$

where Q_i is flow rate (m³ s⁻¹), α is a fitting parameter [ ], Δp is the pressure difference (Pa), W is the channel width (m), E is the substrate elastic modulus (Pa), and h_0 is the initial channel height (m).

The spread of the fitting parameter is too significant to formulate an analytical equation for ϕ that provides an adequate fit for all data. Nevertheless, the use of the fitting parameter (ϕ) from the plateau at the largest height-to-width ratio for each chip provides an adequate fit (see figure 5). This further reinforces the conclusion that the length-to-width ratio dominates
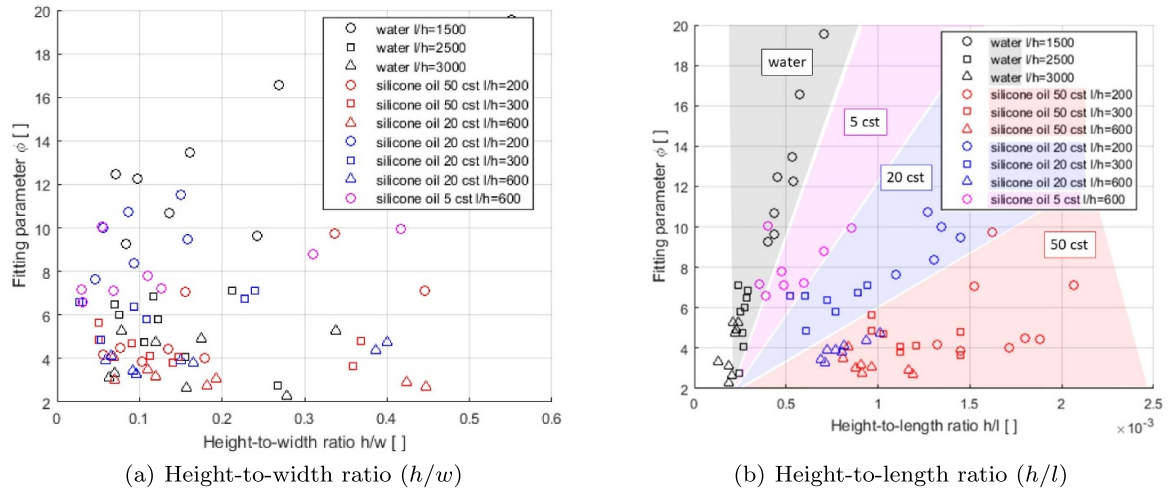
(a) Height-to-width ratio (h/w)

(b) Height-to-length ratio (h/l)

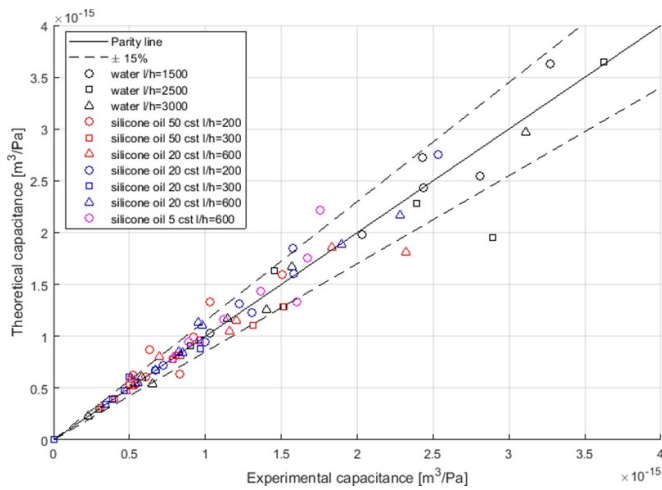**Figure 4.** Fitting parameter (ϕ) relationship with geometric ratios for all fluids.

Figure 5. Assessment of fit for the fitting parameter (ϕ) as a function of the chip only. This does not consider variations in width-to-height ratio; the smallest ϕ value for each chip is used.

3.3. Limitations and uncertainties

The geometric range of conditions is limited to the height, width, and length considered. Any extrapolation cannot be supported. Nevertheless, the dimensions are representative of a wide range of microfluidic chip designs. Moreover, the wide range of viscosity of the fluid used (from 1 cst to 50 cst) covers the usual experimental parameters. Additionally, only PDMS chips are considered. However, the material is ubiquitous in

the microfluidic field. The most common ratio of 10–1 is selected to ensure a wide extent of the results. Finally, the flow rates and pressures considered cover a limited range. The step pressure is up to 200 mbar. This is a typical pressure for the active droplet control platform.

There are multiple sources of uncertainties that lead to data scattering. Nevertheless, the scattering is expected to mimic the typical use of microfluidic chip in everyday settings. For a smaller flow rate (as shown in figure 2), the noise is more significant but still adequate. The first-order fit considers an averaged value within the noise. The hysteresis of the system leads to differences between the time constant from increasing and from decreasing steps. However, the time constant is averaged over both increasing and decreasing steps. The inlets are manually punched. Therefore, their location is not well controlled. The variation between the chips of the same nominal dimensions is attributed to that. A more important factor related to the inlet is its effect on the system capacitance and the debris accumulation.

The sample tubing is inserted in the microfluidic chip through a press fit. Although dust and other debris are cleaned during the manufacturing procedure, the insertion of the tubing creates small PDMS debris within the microchannel network. If enough debris accumulate around the inlet, the resistance of the region is significantly increased. Moreover, the height depends on the location of the inlet as the top channel wall deforms with the tubing insertion. The effects on the time constant could be significant. The uncertainties related to the inlet are challenging to control, their variations are expected to similarly impact every day of microfluidic chips.

Finally, the fitting parameter (ϕ) cannot be expressed succinctly as a function of geometric parameters only. In order to do so, the contribution from the inlet would need to be taken into account to limit the data scattering. Moreover, the flow rate also seems to play an important role; the fitting parameter more strongly correlates with the channel length and the fluid viscosity.

over the height-to-width ratio. Even without considering the height-to-width ratio within the chip-specific data set, a prediction window of $\pm 15\%$ is achieved. However, each fitting parameter used is specific to the chip. A consensus across the various chips could not be achieved.

4. Concluding remarks

4.1. Conclusion

The microfluidic chip compliance is considered separately from the sample tubing compliance. The time constant and chip resistance are experimentally determined from measured input pressure and output flow rate. Then, the capacitance is retrieved by assuming a symmetric RC circuit. The height-to-width ratio and height-to-length ratio are varied with different chip designs that are used with various fluids.

The experimental capacitance is compared to a theoretical formula. The accuracy is within one order of magnitude that is much closer than previous approximations. The fitting parameter (ϕ) exhibits a stronger relationship with the height-to-length ratio than for the height-to-width ratio. The purposeful design of the height-to-width ratio enables the minimization of the capacitance; the height-to-width ratio should be larger than 0.2. As for the channel length, the longer channels minimize the fitting parameter, and thus, the capacitance. For the same pressure step, longer channels have smaller flow rates, smaller volume displacement, and thus, smaller capacitance.

4.2. Future work

The results herein presented are exploratory. Further work should aim to improve the understanding of the microfluidic chip capacitance. A more extended study with wider pressure and flow rate range would extend the findings to more conditions. Moreover, the material properties should be varied to investigate their effects. Different more rigid materials such as polymethyl methacrylate or polycarbonate might eliminate the compliance effects. However, it would also be beneficial to explore the relationship between the capacitance and the PDMS ratio.

Moreover, further experiments should decouple the inlet and channel capacitance for a more detailed understanding. For the channels only, glued capillaries directly connecting to the channel would avoid the need for inlets.

Finally, the experimental setup with the pressure sensor at the inlet and flow sensor at the outlet could be supplemented by another flow sensor at the inlet. The flow rate difference between the two flow sensors could then be attributed to the deformation of the microfluidic chip. The timing and synchronization between the sensors are crucial.

Data availability statement

The data that support the findings of this study are available upon reasonable request from the authors.

Acknowledgment

Author contributions

MH participated in the conceptualization, data curation, formal analysis, investigation (performing the experiments), methodology, project administration, validation, and writing.

JPH and CLR participated in the conceptualization, methodology, and the review and editing of the manuscript.

Conflict of interest

The authors declare that they have no conflict of interest.

ORCID iDs

Marie Hébert ⬤ https://orcid.org/0000-0002-2856-4858
Jan Huissoon ⬤ https://orcid.org/0000-0001-5386-2366
Carolyn L Ren ⬤ https://orcid.org/0000-0002-9249-7397

References

Bruus H 2008 *Theoretical Microfluidics* vol 18 (Oxford: Oxford University Press)

Cartas Ayala M A 2013 Hydrodynamic resistance and sorting of deformable particles in microfluidic circuits *PhD Thesis* Massachusetts Institute of Technology

Christov I C, Cognet V, Shidhore T C and Stone H A 2018 Flow rate-pressure drop relation for deformable shallow microfluidic channels *J. Fluid Mech.* **841** 267–86

Courtney M, Chen X, Chan S, Mohamed T, Rao P P and Ren C L 2016 Droplet microfluidic system with on-demand trapping and releasing of droplet for drug screening applications *Anal. Chem.* **89** 910–5

Fu Y, Li C, Lu S, Zhou W, Tang F, Xie X S and Huang Y 2015 Uniform and accurate single-cell sequencing based on emulsion whole-genome amplification *Proc. Natl Acad. Sci.* **112** 11923–8

Gervais T, El-Ali J, Günther A and Jensen K F 2006 Flow-induced deformation of shallow microfluidic channels *Lab Chip* **6** 500–7

Hebert M, Huissoon J and Ren C L 2022 A perspective of active microfluidic platforms as an enabling tool for applications in other fields *J. Micromech. Microeng.* **32** 043001

Johnston I, McCluskey D, Tan C and Tracey M 2014 Mechanical characterization of bulk Sylgard 184 for microfluidics and microengineering *J. Micromech. Microeng.* **24** 035017

Kim Y, Song J, Lee Y, Cho S, Kim S, Lee S-R, Park S, Shin Y and Jeon N L 2021 High-throughput injection molded microfluidic device for single-cell analysis of spatiotemporal dynamics *Lab Chip* **21** 3150–8

Lefevre F, Chalifour A, Yu L, Chodavarapu V, Juneau P and Izquierdo R 2012 Algal fluorescence sensor integrated into a microfluidic chip for water pollutant detection *Lab Chip* **12** 787–93

Liu P *et al* 2021 Three dimensionally printed nitrocellulose-based microfluidic platform for investigating the effect of oxygen gradient on cells *Analyst* **146** 5255–63

Luo G, Du L, Wang Y and Wang K 2019 Recent developments in microfluidic device-based preparation, functionalization and manipulation of nano-and micro-materials *Particuology* **45** 1–19

Patinglag L, Sawtell D, Iles A, Melling L M and Shaw K J 2019 A microfluidic atmospheric-pressure plasma reactor for water treatment *Plasma Chem. Plasma Process.* **39** 561–75

Qin D, Xia Y and Whitesides G M 2010 Soft lithography for micro- and nanoscale patterning *Nat. Protocols* **5** 491–502

Shembekar N, Chaipan C, Utharala R and Merten C A 2016 Droplet-based microfluidics in drug discovery, transcriptomics and high-throughput molecular genetics *Lab Chip* **16** 1314–31

Waghwani B B, Ali S S, Anjankar S C, Balpande S S, Mondal P and Kalambe J P 2020 *In vitro* detection of water contaminants using microfluidic chip and luminescence sensing platform *Microfluidics Nanofluidics* **24** 1–12

Wang Z, Volinsky A A and Gallant N D 2014 Crosslinking effect on polydimethylsiloxane elastic modulus measured by custom-built compression instrument *J. Appl. Polym. Sci.* **131** 41050

Wong D and Ren C L 2016 Microfluidic droplet trapping, splitting and merging with feedback controls and state space modelling *Lab Chip* **16** 3317–29

Zhang Y, Tseng T-M and Schlichtmann U 2021 Portable all-in-one automated microfluidic system (PAMICON) with 3d-printed chip using novel fluid control mechanism *Sci. Rep.* **11** 19189